A Scattering Center Model for SAR Imagery*

Yeliz Akyildiz and Randolph L. Moses

Department of Electrical Engineering, The Ohio State University

ABSTRACT

We present a high frequency model for scattering present in SAR imagery. The model retains dominant terms of the electromagnetic scattering response of canonical scattering objects using solutions from both Physical Optics and the Geometric Theory of Diffraction. Both frequency and aspect dependence of scattering centers are modeled. It is applicable to single polarization as well as multiple polarization data, and it provides an effective, physics-based description of complex SAR imagery. The model parameters provide a concise, physically relevant description of a complex object and are thus good candidates for use in target recognition, radar data compression, and scattering phenomenology studies. Algorithms for estimating the parameters from measured SAR imagery are presented, and the problem of model structure selection is addressed.

Keywords: synthetic aperture radar, feature extraction, scattering centers

1. INTRODUCTION

Synthetic aperture radar (SAR) provides all-weather, day-or-night remote sensing for mapping, search-and-rescue, mine detection, and target recognition.[1] For SAR data processing applications, it is of interest to represent the high-dimensional image data by a low-dimensional model. The low-dimensional model is useful both for data compression needed for storage or transmission of SAR data, and the model parameters can serve as features for use in object classification.

In this paper we consider an *attributed scattering center* model as a representation of object backscatter in high frequency SAR imagery. At high frequencies, the radar backscatter from an object is well-approximated as the sum of responses from individual scattering centers on the object.[2] Therefore, scattering center descriptions are good candidates for model-based image compression and automatic target recognition (ATR) in high-frequency SAR target classification systems. The attributed scattering center model we consider includes both frequency and aspect dependence of scattering by retaining dominant terms in electromagnetic scattering solutions of canonical objects.[3–5] The frequency and aspect dependence in the model permits discrimination among a number of scattering primitives. In addition, the model describes SAR backscatter from either single or multiple polarization data.

This paper focuses on estimating parameters in the attributed scattering center model from measured SAR imagery. We report refinements of nonlinear least squares minimization procedures developed earlier.[4,6,7] We also present algorithms and insights on two structure selection techniques for discriminating between localized and distributed scattering centers in the model. Significantly, the model parameters are estimated directly from SAR image chips. Processing on image chips facilitates insertion into SAR ATR data processing streams, because post-detection processing is often applied to small chips containing detected regions of interest. In addition, by model fitting only on regions of the image, we realize robustness to assumed clutter models; for example, we reduce uncertainty or bias in feature estimates that might be caused by large nearby clutter scattering that is not well modeled as Gaussian noise. Finally, image-domain processing significantly reduces computational complexity.

An outline of the paper is as follows. Section 2 presents the SAR image formation models and the attributed scattering center model. Section 3 discusses an algorithm for parameter estimation from measured SAR imagery. Section 4 considers structure selection and presents two algorithms for selecting model structure. Section 5 presents numerical results. Section 6 concludes the paper.

*This work was sponsored by the US Air Force Materiel Command under contract F33615-97-1020. The views and conclusions contained herein are those of the authors and should not be interpreted as necessarily representing the official policies or endorsements, either expressed or implied, of the Air Force Research Laboratory or the U.S. Government.

2. THE ATTRIBUTED SCATTERING MODEL

In this section we present a parametric model for the sensor data based on high-frequency approximation of electromagnetic scattering.[4,3,5] The model gives a statistical tool for compression of image data. The scattering model, together with the known sensor and image formation transfer functions, specifies a probabilistic model for the measured image conditioned on the hypothesis.

We consider a data collection scenario consistent with synthetic aperture radar (SAR) imaging. A reference point on the SAR scene is defined, and the radar trajectory is assumed to be co-planar with the reference point. This plane, the imaging plane, is labeled using an $x-y$ Cartesian coordinate system with origin at the reference point and with positive x-direction defined as downrange from the radar at the center of the aperture. The radar position is then described by an angle ϕ defined counterclockwise from the x direction. Far zone backscatter is assumed, and therefore plane-wave incidence is obtained on illuminated objects.

2.1. Scattering Model

From the geometric theory of diffraction (GTD),[2,8] if the wavelength of the incident excitation is small relative to the object extent, then the backscattered field from an object consists of contributions from electrically isolated scattering centers. The backscattered field of an individual scattering center is described as a function of frequency f and aspect angle ϕ, and the total scattered field from a target is then modeled as the sum of these individual scatterers.[5]

$$E(f,\phi;\theta) = \sum_{i=1}^{n} E_i(f,\phi;\theta_i) \tag{1}$$

where $\theta^T = [\theta_1^T, \ldots, \theta_n^T]$ and

$$E_i(f,\phi;\theta_i) = A_i \cdot \left(j\frac{f}{f_c}\right)^{\alpha_i} \exp\left(\frac{-j4\pi f}{c}(x_i\cos\phi + y_i\sin\phi)\right) \operatorname{sinc}\left(\frac{2\pi f}{c}L_i\sin(\phi-\bar{\phi}_i)\right) \exp(-2\pi f\gamma_i\sin\phi) \tag{2}$$

Here, f is frequency, f_c is the radar center frequency, ϕ is aspect angle, and $c = 3\times10^8$ m/sec is the propagation velocity. Each term $E_i(f,\phi;\theta_i)$ represents a single scattering center. The parameters x_i and y_i are the downrange and crossrange locations, A_i is the scattering center amplitude, and $\alpha_i \in [-1,-0.5,0,0.5,1]$ describes the frequency dependence. For multiple polarizations, A_i is a vector whose length is the number of polarization measurements available.

The remaining three parameters (γ_i, L_i, and $\bar{\phi}_i$) define the aspect dependence of the scattering. There are two types of scattering centers: localized and distributed. Localized scattering centers have localized returns in the SAR image. Distributed scattering centers have scattering responses that often span several image pixels. For localized scattering centers, $L_i = \bar{\phi}_i = 0$ and γ_i represents the (small) angle dependence of the response. For distributed scattering centers, $\gamma_i = 0$ and L_i models the length of the scattering center and $\bar{\phi}_i$ its orientation angle.

The parameters α and L in the model distinguish among several scattering geometries. The length L determines if the scattering center is localized or distributed, while the frequency dependence relates to the curvature of the scattering primitive; one obtains $\alpha = 1$ for flat surface scattering, $\alpha = \frac{1}{2}$ for singly-curved surfaces, and $\alpha = 0$ for doubly-curved surfaces. Table 1 shows how the α and L parameters differentiate between several canonical scattering shapes.

The model in (1)–(2) is based on GTD and physical optics approximations for scattering behavior and, while parsimonious, is able to describe a large class of scatterers. The model generalizes the more common point scattering model, which includes neither frequency or aspect dependence of scattering centers (the point scattering model is a special case of (1)–(2) with $\alpha_i = L_i = \gamma_i = 0$). Physical behaviors not well modeled by (1)–(2) for small n include creeping waves and cavity scattering.[5]

Scattering Geometry	α	L
Dihedral	1	$L > 0$
Trihedral	1	$L = 0$
Cylinder	1/2	$L > 0$
Sphere	0	$L = 0$
Edge Broadside	0	$L > 0$
Edge Diffraction	$-\frac{1}{2}$	$L > 0$
Corner Diffraction	-1	$L = 0$

Table 1. Discrimination of canonical scattering shapes from α and L parameters

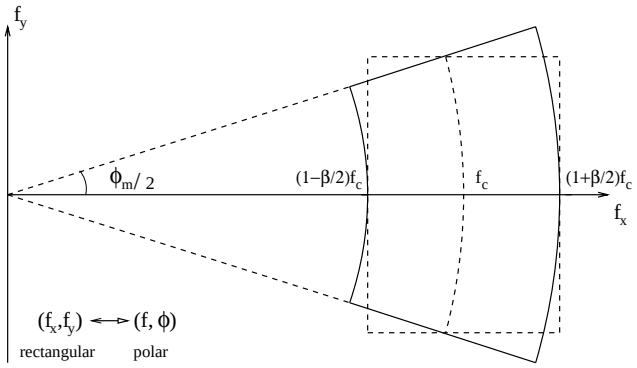

Figure 1. SAR Data Collection Range

2.2. Image Formation

The radar data is collected over a range of frequencies and aspect angles which correspond to a slice in the polar plane, as seen in Figure 1.

The data collection is taken over a frequency range from $f_c \cdot (1 - \beta/2)$ to $f_c \cdot (1 + \beta/2)$ where β is the relative bandwidth and f_c is the center frequency, while the aspect angle changes between $-\phi_m/2$ and $\phi_m/2$. The measured data are uniformly sampled in both f and ϕ.

We assume the SAR image formation processing is as follows. First, the data are resampled to a uniform grid on a Cartesian coordinate space (f_x, f_y) where

$$f_x = f\cos(\phi) \qquad f_y = f\sin(\phi) \tag{3}$$

After resampling, we have samples $E(f_x, f_y)$ on a grid of M samples of $f_x \in [f_c \cdot (1 - \beta/2), f_c \cdot (1 + \beta/2)]$ and N samples of $f_y \in [-f_c \sin(\phi_m/2), f_c \sin(\phi_m/2)]$ that lie inside the rectangle shown in Figure 1

To form the SAR image, we multiply the sampled $E(f_x, f_y)$ by a two-dimensional window function $W(f_x, f_y)$, zero pad to $M_z \times N_z$ samples, and compute the two-dimensional inverse discrete Fourier transform. The result is a complex-valued image $E(x, y)$ defined on an $M_z \times N_z$ array of points. The downrange and crossrange dimensions of each pixel in the array are given by:

$$p_x = \frac{1}{f_c} \cdot \frac{c}{2\beta} \cdot \eta_x, \qquad p_y = \frac{1}{f_c} \cdot \frac{c}{4\sin(\phi_m/2)} \cdot \eta_y \tag{4}$$

where

$$\eta_x = \frac{M-1}{M_z - 1}, \qquad \eta_y = \frac{N-1}{N_z - 1} \tag{5}$$

are factors that correspond to the effect of zero padding in image formation.

3. PARAMETER ESTIMATION

Given a SAR image $D(x,y)$ which is formed from frequency samples $D(f_x,f_y)$ using the imaging model of the previous section, we wish to estimate the order n and the parameter vector $\theta^T=[\theta_1^T,\ldots,\theta_n^T]$ that best describe the data using some goodness of fit measure. We adopt a statistical measure of goodness of fit, in which we assume the measurements $D(f_x,f_y)$ can be approximated as a sum of a scattering term that fits the assumed model and a Gaussian noise term:

$$D(f_x,f_y)=E(f_x,f_y;\theta)+N(f_x,f_y) \tag{6}$$

where $E(f_x,f_y;\theta)$ represents the model in (1) on a Cartesian frequency grid, and $N(f_x,f_y)$ is zero mean Gaussian noise. We then seek maximum likelihood parameter estimates.

Maximum likelihood parameter estimates are found from the solution to a nonlinear least squares problem. The solution can be obtained directly from image-domain measurements. The image formation process can be represented by a linear operator B. Stacking the image-domain measurements $D(x,y)$ into a $K\times 1$ vector d, we have

$$d=B\tilde{d}=B\left[\tilde{e}(\theta)+\tilde{n}\right]=B\left(\sum_{i=1}^{k}\tilde{e}_i(\theta_i)\right)+n \tag{7}$$

where $\tilde{d}$, $\tilde{e}(\theta)$, $\tilde{e}_i(\theta_i)$, and $\tilde{n}$ are vectors whose elements are measurements, scattering model, scattering center components and noise in the Cartesian frequency domain (f_x,f_y), respectively. The vector n represents the noise in the image domain. If $\tilde{n}\sim\mathcal{N}(0,\tilde{\Sigma})$, then $n\sim\mathcal{N}(0,\Sigma)$ with $\Sigma=B\tilde{\Sigma}B^H$.

The maximum likelihood estimate of θ is the vector that minimizes the negative log likelihood function:

$$\hat{\theta}_{ML} = \arg\min_{\theta} J(\theta) \tag{8}$$

$$J(\theta) = [d-e(\theta)]^H\Sigma^{\dagger}[d-e(\theta)] \tag{9}$$

where $(\cdot)^H$ denotes Hermitian transpose, $(\cdot)^{\dagger}$ denotes Moore-Penrose pseudoinverse, and $e(\theta)$ is the scattering model vector in the image domain. Equation (8) is a nonlinear least squares minimization problem; because d and θ are of high dimension, direct minimization is computationally intensive, and we seek computationally simpler suboptimal solutions.

We make use of the fact that scattering center responses are localized in the image domain. The above minimization can be approximately decomposed into smaller estimation problems. We partition the image $D(x,y)$ into r regions R_k of high energy and a remainder region R_0. Defining Π_k as the projection onto region R_k, we have

$$\begin{aligned} J(\theta) &= \sum_{k=0}^{r}[d-e(\theta)]^H\Pi_k\Sigma^{\dagger}\Pi_k[d-e(\theta)] \\ &\approx \sum_{k=1}^{r}[d-e(\theta^k)]^H\Pi_k\Sigma^{\dagger}\Pi_k[d-e(\theta^k)]+C \end{aligned} \tag{10}$$

where $\theta^k=[\theta_{i_1}^T,\ldots,\theta_{i_{l(k)}}^T]^T$ is a vector containing the scattering parameters for region R_k and C is a constant independent of θ. We see that each region R_k is modeled by $l(k)$ scattering centers, where $\sum_{k=1}^{r}l(k)=n$. Since the number of pixels in R_k is (much) less than K and the θ^k form a disjoint partition of θ, the individual minimization problems in equation (10) are decoupled and of (much) smaller size.

We employ a sequential segmentation process based on a watershed algorithm to isolate regions of high energy in the image.[9] The algorithm operates by treating the magnitude of the SAR image as a three-dimensional landscape under water. As the water is drained, the largest peak surfaces first, and is assigned as segment 1. The draining process continues until the -3 dB level is reached, and each local maxima surfacing is assigned to a new segment. If two or more segments meet, they are combined; this prevents shallow ripples being assigned to different segments. After reaching the -3 dB level, we only focus on the segment containing the largest peak and grow the region until the -20 dB level. We do not include any pixels with magnitudes less than 20 dB below the peak, assuming they are mainly due to clutter.

Having identified the segment containg the largest peak, local feature extraction is applied. After the processing of the segment is completed, it is removed from the image. The whole segmentation algorithm is repeated to determine the next region to be processed.

3.1. Parameter Normalization

To improve the numerical properties of the nonlinear minimization, and to provide a resolution-independent description of the model, we normalize the model parameters in the following way. We define

$$x_p = \frac{x}{p_x} \qquad y_p = \frac{y}{p_y} \qquad L_p = \frac{L}{p_y} \qquad \gamma_p = \gamma 4\pi f_c \sin(\phi_m/2) \qquad \overline{\phi}_p = \frac{\overline{\phi}}{\phi_m/2} \tag{11}$$

The parameters x_p, y_p, and L_p are normalized by the downrange and crossrange pixel spacing of the SAR image. The new parameter $\overline{\phi}_p$ ranges from -1 to 1, representing the tilt angle as a percentage of the maximum aperture. The parameter γ_p specifies the dispersion as a function of aspect angle. For example, $\gamma_p = 1$ means that as we go from the left extreme of the aperture to the right extreme, the amplitude changes by a factor of e^1. In addition, we define

$$L_c = L \cdot \frac{4f_c \sin(\phi_m/2)}{c} = \frac{L_p}{\eta_y} \tag{12}$$

The length L_c is normalized to the (minimum) crossrange resolution of the SAR system, and unlike L_p is independent of the amount of zero padding used.

We further normalize and scale the Cartesian frequencies as

$$f_{xn} = \frac{f_x}{f_c} \qquad f_{yn} = \frac{f_y}{f_c} \qquad f_2 = \frac{f_{yn}}{2\sin(\phi_m/2)} \tag{13}$$

With these normalizations, $f_{xn} \in [1-\beta/2, 1+\beta/2]$, $f_{yn} \in [-\sin(\phi_m/2), \sin(\phi_m/2)]$, and $f_2 \in [-1/2, 1/2]$. In the normalized terms, each scattering center model is

$$\begin{aligned} E(f_{xn}, f_{yn}) \quad = \quad & A \cdot (j\sqrt{{f_{xn}}^2 + {f_{yn}}^2})^{\alpha} \cdot \operatorname{sinc}\left(\frac{\pi\sqrt{{f_{xn}}^2 + {f_{yn}}^2} L_p \eta_y}{2\sin(\phi_m/2)} \sin\left(\tan^{-1}(f_{yn}/f_{xn}) - \overline{\phi}_p \phi_m/2\right) \right) \\ & \cdot \exp(-f_2\gamma_p) \cdot \exp\left(-j2\pi\left(\frac{f_{xn}}{\beta} x_p \eta_x + f_2 y_p \eta_y\right)\right) \end{aligned} \tag{14}$$

We implement the nonlinear minimization using the above normalized model. The benefits are: i) better numerical conditioning of the minimization process, because the individual parameters are normalized, and ii) modularity of the model fitting code, because it is independent of center frequency, bandwidth, or SAR aperture integration angle, and dependent only on normalized versions of these parameters.

3.2. Algorithm Implementation

As a result of the segmentation process, we obtain regions of high energy to perform the feature extraction algorithm. The first step of the algorithm is to classify the segment of interest as a distributed scattering mechanism or a localized scattering mechanism. The details of the structure selection procedure are discussed in Sections 4 and 5.

After classification, we need to obtain the ML estimates of the model describing that scattering center. The minimization of the cost function, $J(\theta)$ is a high dimensional, nonlinear optimization problem. The cost function typically has several local minima, so good parameter initialization is essential to descend to the global optimum solution. The parameters $\{x_p, y_p, \alpha, \gamma_p, L_p\}$ are initialized using the methods described in Koets,[6] and $\overline{\phi}_p$ is initialized to zero. With this starting point, the BFGS Quasi-Newton method, using both quadratic and cubic line search algorithms is implemented and the ML estimates are obtained; we use the MATLAB command `fminu.m` to perform the minimization. The processed segment is removed from the image and the segmentation process is repeated to extract the next scattering center. The process terminates when a user specified amount of peaks are processed, the peak value of the current region is less than 20 dB below the largest peak of the image or more than a specified percent of the original energy is already modeled.

The Cramér-Rao bound (CRB) on estimator variance for the parameters of the attributed scattering center model has been derived.[4,6] The nonlinear least squares algorithm has been applied to both synthetic and measured imagery, and is shown to give parameter estimates that are close to the CRB in a number of cases.[4,6,7]

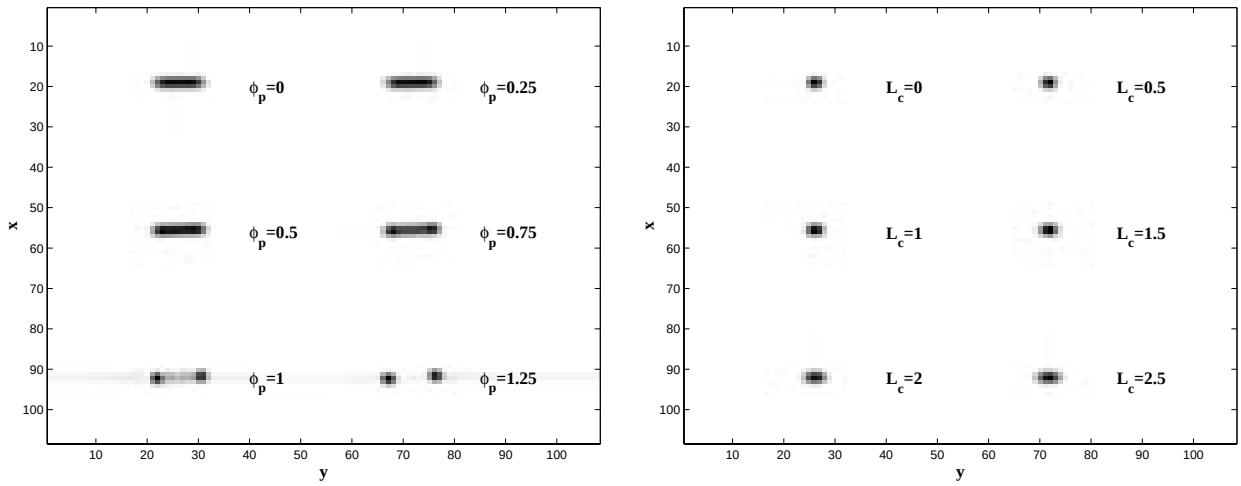

(a) (b)

Figure 2. SAR images for distributed scatterers and localized scatterers may be very similar for some parameter choices.

4. STRUCTURE SELECTION

In this section we investigate model structure selection. In particular, each scattering center is described by one of two possible models, a localized scattering model ($L = 0$) or a distributed scattering model ($L > 0$). The parameters in the model are different for the two cases. For a localized scattering center, $L = 0$ and $\overline{\phi}$ is undefined, so the parameter vector is $\theta = [x, y, A, \alpha, \gamma]$. For a distributed scattering center, $L > 0$; in this case $\gamma = 0$ and the parameter vector is $\theta = [x, y, A, \alpha, L, \overline{\phi}]$. An issue in the parameter estimation problem is how to choose between the two structures. Previous parameter estimation algorithms[4,6] either assume the structure is known or estimate the structure from the image segmentation. In this section we consider a GLRT approach to structure selection as well as a computationally simpler image-based approach. In Section 5 we study the performance of the two techniques.

One difficulty in structure selection is that a localized scattering center is well-modeled as a distributed scattering center with $L \approx 0$. In addition, a distributed scattering center is well-modeled as two localized scattering centers. The models do not exactly coincide except in the case that a localized scattering center with $\gamma = 0$ is identical to a distributed scattering center with $L = 0$ and any choice of $\overline{\phi}$. Thus, the parameters are in most cases identifiable; however, the differences between these models is small, so noisy data can be well-modeled by both choices. Thus, for measured SAR images with clutter present, it may be difficult or impossible to reliably distinguish between a localized and a distributed scattering center.

The identifiability problem is illustrated in Figure 2. Figure 2(a) shows SAR images for a distributed scattering center with $L_c = 6$ for various values of $\overline{\phi}_p$. We see that the response in the image appears as a single distributed scattering center for $|\phi_p| < 1$, but appears as two localized scattering centers for $|\phi_p| > 1$. Figure 2(b) shows SAR images for distributed scattering centers with $\overline{\phi}_p = 0$ and various values of L_c. The image for $L_c = 0$ is identical to the image of a localized scattering center with $\gamma = 0$. We see that for small L_c, the response becomes indistinguishable from a localized scattering center.

We use the following terminology for our structure selection problem. We assume two possible hypotheses for the structure corresponding to a region R_k in the SAR image: either H_ℓ if the scattering center is a single localized response ($L = 0$), or H_d if the scattering center is a single distributed response ($L > 0$). We define the probability of false alarm P_{FA} as the probability of selecting a distributed scattering center when the true scattering center is localized, and define the probability of detection P_D as the probability of correctly selecting a distributed scattering center.

Below we propose two tests for structure selection. The first is a generalized likelihood ratio test (GLRT). The second is a computationally simple test based on the extent of the high-energy response in the SAR image.

4.1. GLRT Structure Selection

Assume we have identified a region R_k of the SAR image to be modeled as either a single distributed scattering center or a single localized scattering center; the region is determined from the watershed segmentation algorithm discussed in Section 2. Let d denote a vector of measured SAR image pixels from that region. We fit both a localized scattering model and a distributed scattering model using the nonlinear least squares procedure in Section 3. Let $\hat{\theta}_\ell$ and $\hat{\theta}_d$ denote the parameter vector obtained from the localized and distributed fitting, respectively. We form the model errors

$$e_\ell = \|d - s(\hat{\theta}_\ell)\|_Q, \qquad e_d = \|d - s(\hat{\theta}_d)\|_Q \tag{15}$$

where $s(\hat{\theta}_\ell)$ and $s(\hat{\theta}_d)$ are the reconstructed image pixel vectors using the estimated localized and distributed models, respectively, and $\|v\|_Q = v^H Q v$ for some positive semidefinite matrix Q; if $Q = \Pi_k \Sigma^\dagger \Pi_k$ the model errors in (15) are negative log likelihoods corresponding to the respective parameter estimates; see (10). The GLRT structure selection test is then given by

$$\frac{e_\ell}{e_d} \underset{\mathrm{H}_\ell}{\overset{\mathrm{H}_\mathrm{d}}{\gtrless}} \eta_{GLRT} \tag{16}$$

where η_{GLRT} is a user-selectable threshold.

4.2. Image-Based Structure Selection

A computationally simple structure selection test can be derived by exploiting the shape of the scattering center in the SAR image. In particular distributed scattering centers have widths that are larger than the width of a localized scattering center (see Figure 2).

The algorithm we propose is as follows. We extract the crossrange pixel samples in the selected region for the downrange distance corresponding to the peak value in the region. This results in a small number of samples (usually between 3–20) indexed on crossrange location. We normalize these pixels to have a peak value of one and then fit a parabola, $ax^2 + bx + c$ to the samples using a least-squares fit for the parameters (a, b, c). The distance between the zero crossings of the parabola $ax_2 + bx + (c - \alpha)$, where $\alpha = 10^{-\frac{3}{20}}$, forms an estimate $\hat{W}$ of the -3 dB width, of the scattering center, in units of crossrange pixels. The image-based hypothesis test for a localized or distributed scattering center is given by

$$\hat{W} \underset{\mathrm{H}_\ell}{\overset{\mathrm{H}_\mathrm{d}}{\gtrless}} \eta_W \tag{17}$$

where η_W is a user-selectable threshold.

A parabola is chosen because for localized scatterers, the crossrange response is essentially the point spread function of the radar imaging process in the crossrange direction, and for most windows used in radar image formation, this response is well-modeled by a parabola. For a distributed scattering center, the parabola is not as good a fit, but still gives an estimate $\hat{W}$ which is above any threshold η_W chosen for practical false alarm probabilities (see Section 5). In addition, the parabola gives a real-valued estimate of width (and not, *e.g.*, quantized by pixel samples) which is essentially independent of the center locations of the scattering center.

The above test is computationally simpler than the GLRT test, because it avoids fitting the region with two separate models. On the other hand, the algorithm is expected to have inferior performance compared to the GLRT test, because it uses only a subset of the available data and prior information about the scattering center responses.

5. NUMERICAL RESULTS

In this section we evaluate the performance of the two proposed structure detection tests presented in Section 4.

We first present results that quantify the difficulty, in an algorithm-independent way, of the structure selection problem for small L_c. Figure 3 shows the difference in fit error when a distributed and a localized model are used to model a distributed scattering center with true length L_c. For each value of L_c we generate 20 realizations of the scattering center with different center locations (x and y) to account for estimation differences as a function of location. For each realization we fit localized scattering center parameter vector θ_ℓ, and form the reconstructed image pixel vector $s(\theta_\ell)$. We compute the normalized difference $\|s(\theta_\ell) - d\|/\|d\|$, where d is the vector of pixels corresponding to the true model. We also compute $\|n - d\|/\|d\|$, where n is a vector of noise pixels corresponding

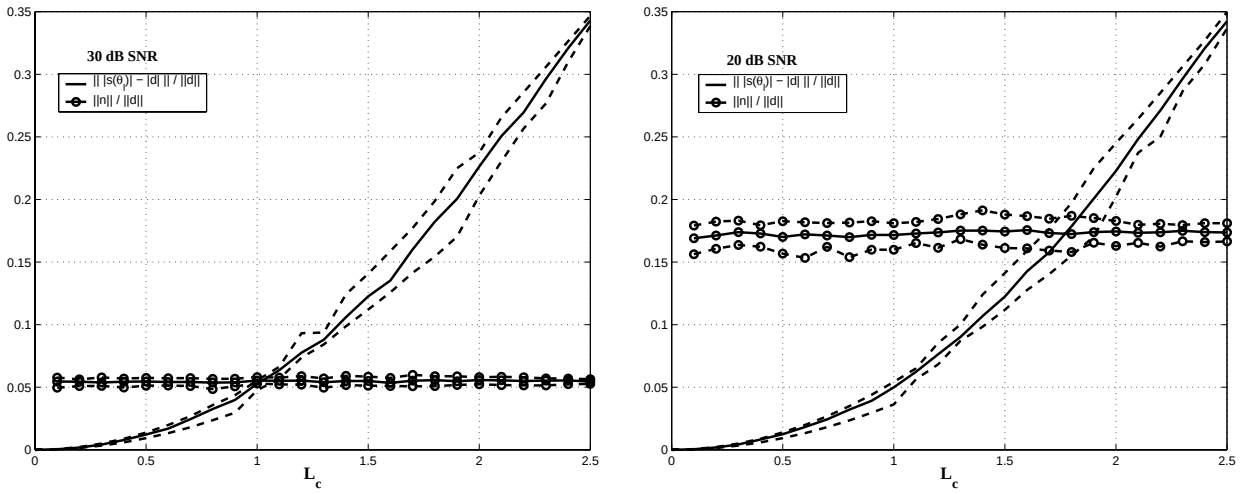

(a) SNR=30 dB (b) SNR=20 dB

Figure 3. Normalized error norms between localized and distributed scattering model for a distributed scattering center with length L_c. Also displayed is the normalized norm of the noise component for two SNR values. The minimum, mean, and maximum norm for 20 realizations are shown.

to a scattering center with SNR of 20 dB or 30 dB. Here, SNR is defined as the ratio of the peak amplitude of the scattering center to the noise standard deviation in the image domain. We plot the minimum, mean, and maximum of these norm ratios for several values of L_c. We expect to be able to discriminate a localized from a distributed scattering center only when the differences in the model norms become greater than the noise component of the norm. As seen in Figure 3, for a signal-to-noise ratio of 30 dB, an L_c value greater than 1.2 is required to reliably detect a distributed scatterer. The threshold increases to $L_c = 1.7$ when the SNR is 20 dB.

Figure 4 shows histograms of the ML $\hat{L}_c$ parameter estimates obtained when the true scattering center is a localized scattering center (denoted $L_c = 0$), and when it is a distributed scattering center with $L_c = 0$, 0.5, 1, and 2. The SNR is 20 dB. We see from the histograms that $f(\hat{L}_c|H_d) \approx f(\hat{L}_c|H_\ell)$ for small L_c values. We start observing a difference when the simulated scattering center has a length $L_c > 1.5$, which is consistent with the results in Figure 3.

Figure 5 shows P_D versus P_{FA} for SNR=20 dB and for the two structure hypothesis tests proposed in Section 4. Both tests perform similarly, and not much better than chance, for $L_c \leq 1$; this is consistent with predictions based on Figure 3(b). For $L_c > 1.5$ the GLRT test performs significantly better than the image-based test. For $L_c \geq 2.5$, both tests give very few errors in structure selection. Thus, the additional computational cost in the GLRT test has the benefit in improved structure selection for L_c between 1 and 2.5.

6. CONCLUSIONS

We have presented an attributed scattering center model for representing objects from SAR imagery. The model includes both frequency dependence and aspect dependence of scattering terms, and as such discriminates between a number of canonical objects. Model parameter estimates are obtained using an approximate maximum likelihood formulation; the high-order estimation problem is decoupled by fitting small-order models on disjoint regions in the SAR image.

We focused on a problem of structure estimation, where we consider whether a region of high energy in the SAR image is to be modeled as a localized or distributed scattering center. For distributed scattering centers with small length, the fit error from using a localized model is small, and may be lower than the background clutter level in the SAR image. We propose two algorithms for structure selection, a GLRT detector and a suboptimal but computationally efficient image-based detector. Simulation results showed that neither algorithm could effectively discriminate between a localized scattering center and a distributed scattering center with small length, especially for low SNR imagery. For long lengths (greater than about 2-2.5 times the crossrange resolution at 20 dB SNR), both algorithms were able to correctly select the correct model structure with very few false alarms. The GLRT test has better performance than the image-based test for scattering center lengths between these two extremes, in

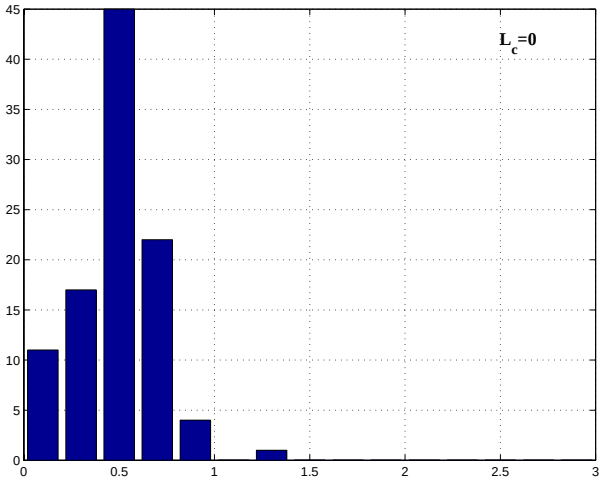

(a) Localized Scatterer (H_ℓ)

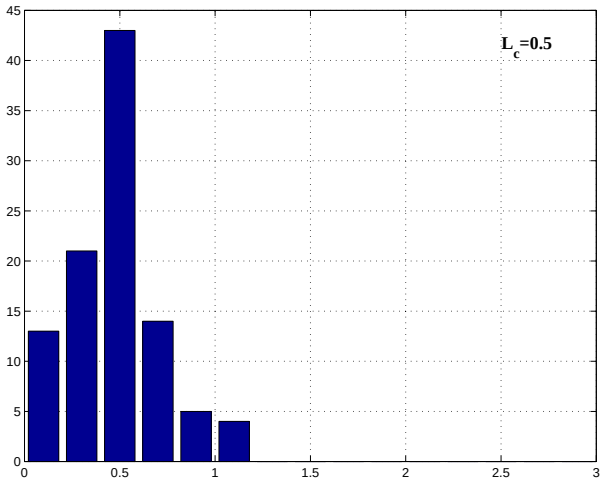

(b) $L_c = 0.5$

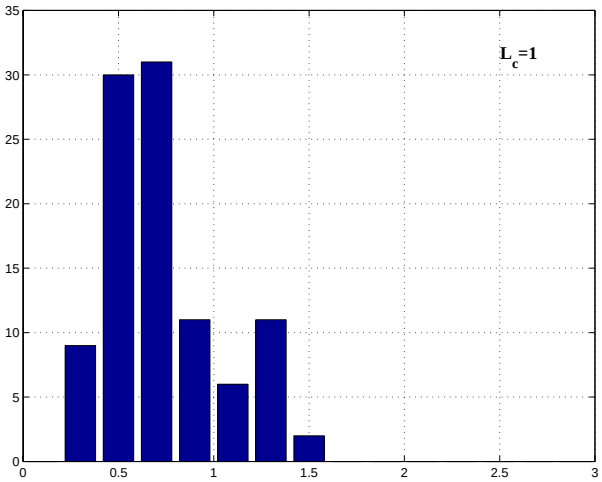

(c) $L_c = 1.0$

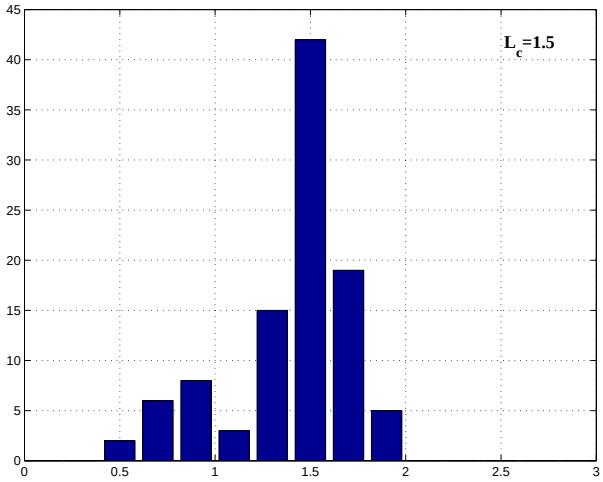

(d) $L_c = 1.5$

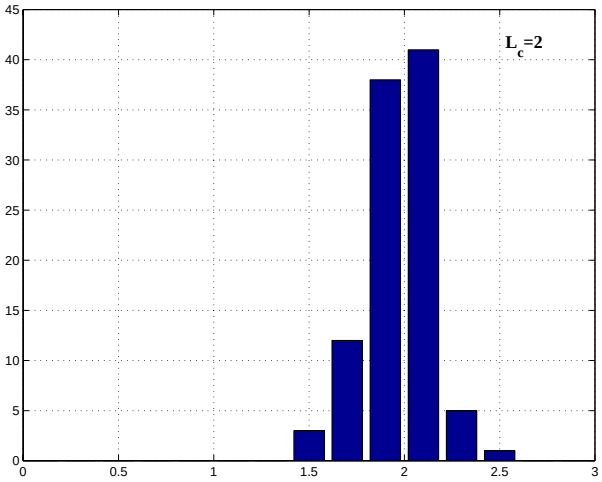

(e) $L_c = 2.0$

Figure 4. Histograms of ML estimate $\hat{L}_c$ under hypothesis H_ℓ (top) and under hypothesis H_d for varying values of L_c. SNR=20 dB.

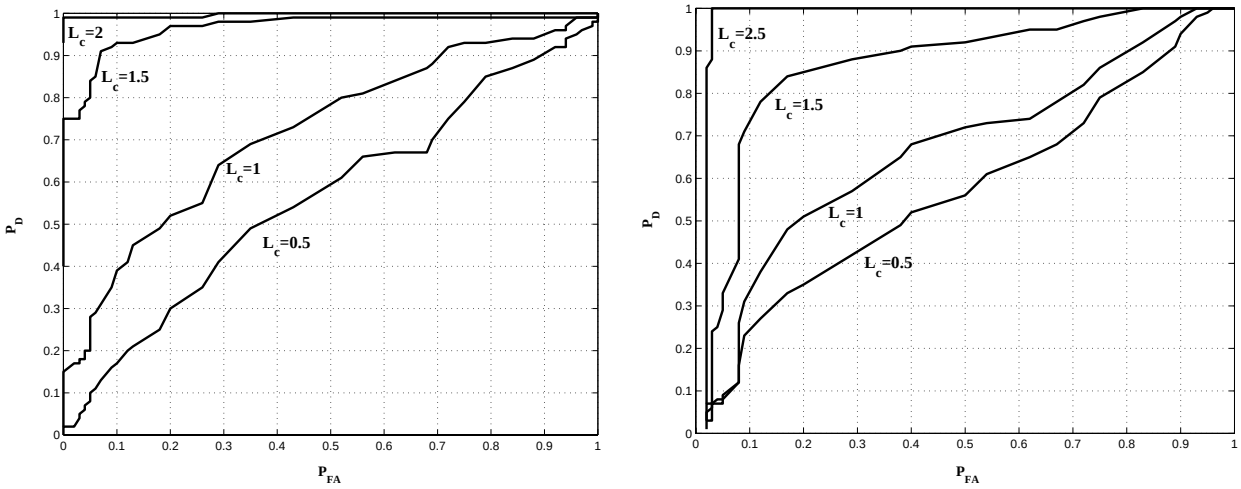

(a) GLRT test (b) Image-based test

Figure 5. Detection versus false alarm probabilities of the two proposed structure selection algorithms for SNR=20 dB.

the region of 1-2.5 times the crossrange resolution (for 20 dB SNR). The price paid for the increased performance is increased computation to implement the GLRT test.

Future work will address structure selection performance for multiple scattering centers, and incorporation of minimum description length principles into the tests.

REFERENCES

1. C. Curlander and R. N. McDonough, *Synthetic aperture radar: systems and signal processing*, Wiley, New York, 1991.
2. J. B. Keller, "Geometrical theory of diffraction," *J. Opt. Soc. Am.* **52**(2), pp. 116–130, 1962.
3. L. C. Potter and R. L. Moses, "Attributed scattering centers for SAR ATR," *IEEE Transactions on Image Processing* **6**, pp. 79–91, January 1997.
4. M. Gerry, *Two-dimensional Inverse Scattering Based on the GTD Model*. PhD thesis, The Ohio State University, Columbus, OH, 1997.
5. M. J. Gerry, L. C. Potter, I. J. Gupta, and A. van der Merwe, "A parametric model for synthetic aperture radar measurements," *IEEE Transactions on Antennas and Propagation* **47**, July 1999.
6. M. Koets, "Automated Algorithms for Extraction of Physically Relevant Features from Synthetic Aperture Radar Imagery," Master's thesis, The Ohio State University, Columbus, OH, 1998.
7. M. A. Koets and R. L. Moses, "Feature Extraction using Attributed Scattering Center Models on SAR Imagery," in *SPIE*, (Orlando, Florida), April 1999.
8. R. G. Kouyoumjian and P. H. Pathak, "A uniform geometrical theory of diffracti for an edge in a perfectly conducting surface," *Proc. IEEE* **62**, pp. 1448–1461, November 1974.
9. J. Stach and E. LeBaron, "Enhanced Image Editing by Peak Region Segmentation," in *Proceedings of the 1996 AMTA Symposium*, October 1996.